



Volume change response and fabric evolution of granular MX80 bentonite along different hydro-mechanical stress paths

Alessio Ferrari^{1,2} · Jose A. Bosch¹ · Patrycja Baryla¹ · Marco Rosone²

Received: 3 June 2021 / Accepted: 21 January 2022 / Published online: 12 February 2022
© The Author(s) 2022

Abstract

Despite the increasing understanding of bentonite behaviour, there is still missing evidence on how different hydro-mechanical loadings, including sequences of hydration and compression, affect the fabric and the volume change behaviour of the material. It is generally assumed that the interplay between the behaviour of clay assemblages and the overall fabric of the material is the reason of having final states that are dependent on the stress path followed. Here the results of an experimental campaign aiming to study these factors are reported and discussed. Free swelling and swelling pressure tests were performed, both followed by compression to a relatively high stress. The experimental program involved various samples that were dismantled at intermediate states in order to perform microstructural observations by means of mercury intrusion porosimetry and electronic scanning microscopy. It was observed that while the void ratio at a given stress level depends on the stress path, subsequent compression led to a unique virgin compression line. The data obtained at the microscale gave further insight for an interpretation of the volume change behaviour observed at the macroscale, showing that at high stress the material tends to recover the same fabric regardless of the path to saturation.

Keywords Bentonite · Clay fabric evolution · Hydro-mechanical response · Pore size distribution · Stress-path dependency · Swelling pressure

1 Introduction

Bentonites have been extensively studied in recent decades for their role as backfill and sealing material for deep geological repositories of nuclear waste. Throughout their use in this context, bentonites will be subjected to a series of processes such as compaction, hydration, swelling in free and/or confined conditions, which will lead to a variety of hydro-mechanical stress paths. Understanding and being able to anticipate the bentonite response under those loadings is a prerequisite to evaluate safety functions of the engineered barrier systems.

It is well known that the behaviour of expansive clays such as bentonites is stress-path-dependent. Lloret et al. [16] reported the results of a comprehensive experimental

program that involved a variety of stress paths in suction-controlled oedometric tests performed on FEBEX bentonite in block form. All tests started from the same initial conditions, and the results showed that samples sharing the final net stress and suction did not have the same final void ratio. Similar observations were made by Wang et al. [32] on compacted MX-80/sand mixed at a dry mass ratio of 70/30; in particular, samples that were allowed to swell during saturation required values of stress to recover the initial void ratio larger than the ones developed in samples in which constant volume was imposed during saturation. The stress-path-dependent behaviour can also be identified at a local scale in laboratory tests such as those presented by Molinero-Guerra et al. [11] on MX-80 bentonite and Liu et al. [15] on GMZ bentonite, both bentonites being initially in the form of pellets/powder mixtures; the tests consisted on wetting under constant volume conditions inside infiltration columns where radial stresses were measured at different heights; the results revealed that local stresses equilibrated at different values depending on the distance to the wetting source.

✉ Jose A. Bosch
jose.boschlufriu@epfl.ch

¹ Ecole Polytechnique Fédérale de Lausanne, Lausanne, Switzerland

² Università Degli Studi Di Palermo, Palermo, Italy

Up to date, the sources of stress-path dependency have been mostly interpreted with a double porosity framework, following the precursory work of Gens and Alonso [10]. Indeed, one of the features of compacted bentonite-based materials is the marked double porosity network [1, 5, 14–16, 20, 25, 28], or even triple porosity, such as that resulting from the use of mixtures of highly compacted pellets (e.g. [12]). Thus, many experimental studies have been devoted to the microstructure of bentonites. Alonso et al. [2] performed mercury intrusion porosimetry (MIP) tests on samples of FEBEX pellets that, sharing the same initial as-compacted state, were subjected to different hydro-mechanical paths. The final pore size distribution (PSD), obtained by means of MIP technique, revealed that the change in microstructure of the bentonite after different hydro-mechanical loadings is the result of the interaction between micro- and macrostructural arrangements. Wang et al. [31] studied the evolution of the pore size distribution of MX80-sand bentonite hydrated under isochoric conditions; MIP tests, performed on samples equilibrated at different values of suction, showed that the most significant changes in PSD were taking place close to saturated conditions. Similar results were obtained by Niu et al. [19] on GMZ bentonite. Seiphoori et al. [25] analysed the evolution of the fabric of granular MX80 bentonite under isochoric conditions, relating it to changes in the water retention behaviour; they performed wetting–drying cycles that led to hysteretic response of the water retention curve; MIP results were obtained at several stages of the wetting–drying cycles showing that the hysteretic water retention behaviour could be related to the evolution of the PSD.

Despite all the valuable information that can be gathered examining the current literature, there is still missing evidence on the evolution of microstructure along different stress paths that have the same initial and final states in terms of stress and suction. This lack of evidence is particularly the case for granular bentonite with optimised apparent grains size distribution, which has an initial fabric different from both pellets and compacted blocks [25]. Whether this initial fabric influences the hydro-mechanical behaviour at saturation is not clear yet. Experimental data remain also necessary in order to improve the knowledge on the sources of the stress-path-dependent response, such as the observed difference of void ratio between samples that share the same stress state, but have reached it through different stress paths starting from as-compacted unsaturated conditions (see, e.g. [10, 16]). This knowledge would be needed to anticipate the homogenisation of the bentonite in a repository, considering that different stress paths would apply to different portions of the barrier at the local scale,

during stress and pore water pressure equilibration towards the steady state.

This paper aims to fill this gap by evaluating the behaviour of the MX80 granular bentonite under two different stress paths, which share the same initial and final degree of saturation, as well as the same initial and final axial stress. The first stress path involved wetting up to saturation under low stress, and the second path considered hydration under constant volume conditions. To complement previous studies [12, 31], both paths were followed by compression up to high stress to clearly visualise the virgin compression curves. The two stress paths are representative of actual repository conditions. Indeed, in a buffer or backfill, a similar path to the first one is expected to develop locally in technological gaps filled with bentonite, which will be hydrated at low or no stress; later, as the hydration front advances towards the centre, the bentonite will be compressed due to the swelling of internal bentonite. The second path is representative of the inner parts of the barrier, in which the surrounding material will limit the volume change of the bentonite upon hydration. The oedometric tests are complemented by microstructural observations at different stages of the stress paths by means of MIP and scanning electron microscopy (SEM). This microstructural investigation is intended to provide further insight on the causes of the observed stress-path-dependent response.

2 Tested material

The material tested was granular MX-80 bentonite, with 85% smectite content, a specific surface of 523 m²/g and a specific gravity of 2.74. The liquid limit is 420%, and

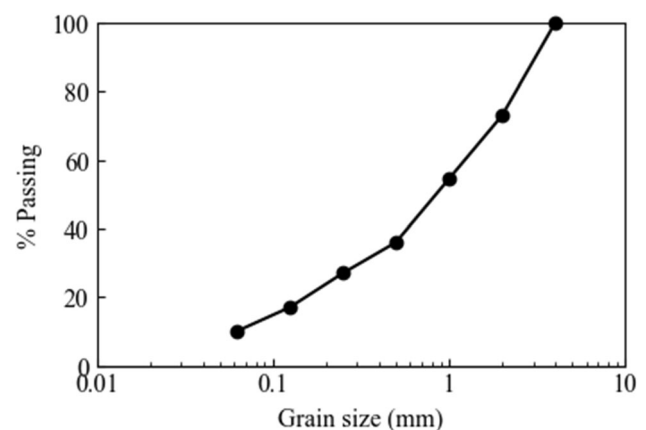


Fig. 1 Apparent grain size distribution of the MX80 granular bentonite

the plastic limit is 65%. This material is composed by grains of compacted bentonite of different sizes, allowing to achieve the apparent grain size distribution (GSD) shown in Fig. 1, which is characterised by a curvature coefficient of $C_C = 1.5$ and a uniformity coefficient of $C_U = 6$. The GSD is designed in order to optimise the emplacement of the bentonite at a dry density (ρ_d) of around 1.5 Mg/m^3 , achieved by pouring the granular mixture (i.e. without compaction energy) [20]. The hygroscopic water content of the granular mixture is in the range of 5–7%.

The dry density of the individual grains is approximately $\rho_d = 2.10 \text{ Mg/m}^3$. Seiphoori [24] reported the initial PSD (computed from the intruded mercury void ratio in MIP test as $-\frac{\Delta e_{Hg}}{\Delta \log d}$) of a single grain as well as the PSD of an as-poured grain mixture (i.e. a sample resulting from pouring the material without any compaction effort) in hygroscopic conditions, which are reproduced in Fig. 2, showing that a single grain has—in the explored range of pore dimension—a unimodal PSD, whereas the mixture shows a bimodal PSD that resembles those reported for as-compacted bentonite at similar dry density (e.g. [16]). The water retention behaviour of this material was studied by Seiphoori et al. [25]. In its as-poured state, with $\rho_d = 1.5 \text{ Mg/m}^3$, the initial degree of saturation was between 20 and 25% and the air entry value was about 5 MPa in terms of total suction. Moreover, in terms of water content versus suction a unique trend until saturation was identified in main wetting paths for different dry densities, indicating that adsorption is the most dominant mechanism of water retention for the studied ranges of dry density ($\rho_d = 1.5 \text{ Mg/m}^3$ to $\rho_d = 1.8 \text{ Mg/m}^3$) and suction (from about 300 MPa to about 1 MPa).

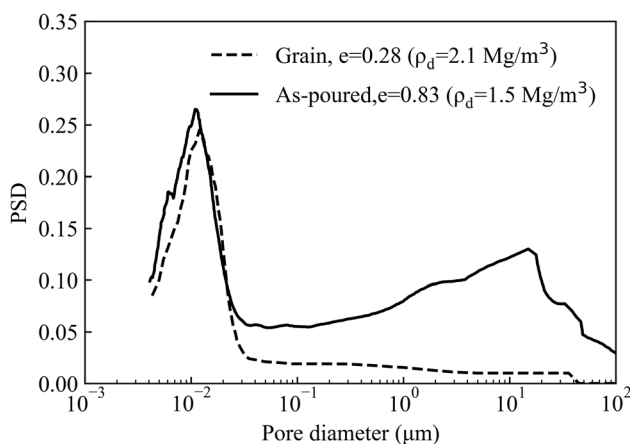


Fig. 2 PSD of the samples in their as-poured state and of a single grain (data from [24])

3 Experimental set-up and testing procedures

A high-pressure oedometric cell was used in order to initially saturate the bentonite samples under both quasi-isochoric conditions and constant axial load, and to apply the subsequent loading steps. Figure 3 shows a scheme of the experimental set-up. A detailed description of the apparatus can be found in [9]. The cell is made of stainless steel and holds an oedometric ring with a height $h = 12.5 \text{ mm}$ and diameter $d = 35.0 \text{ mm}$. This ring contains the bentonite sample. The top and the bottom of the sample are in contact with metallic porous plates, which are connected to the drainage lines, through which water is supplied with two independent pressure/volume (PV) controllers (resolution of pressure control of 1 kPa).

The cell is placed in a high-stiffness frame equipped with a hydraulic jack, allowing to control the axial total stress, σ_a , up to 100 MPa with a resolution of 0.06 MPa. The vertical displacement is measured by LVDTs with a resolution of $1 \mu\text{m}$ fixed on the upper part of the oedometric cell. The application of high confining stress is not instantaneous, and it depends on the performance of the volume/pressure controller connected to the hydraulic jack, the compressibility of the apparatus and the compressibility of the material tested [9].

The samples were prepared by pouring the granular mixtures of MX80 directly into the oedometric ring, with no compaction energy. Six samples were prepared for testing, the initial conditions of which are summarised in Table 1. The values of total suction reported in Table 1 were measured using a chilled-mirror psychrometer apparatus (WP4-T, Decagon device). Samples P1-were saturated at constant stress, whereas samples P2-correspond to those saturated under constant volume conditions.

Inside the oedometer cell, the samples were wetted with distilled and de-aired water, supplied at a constant back-pressure of $u_w = 20 \text{ kPa}$. Two different mechanical conditions were tested during wetting, leading to two different stress paths. The first stress path (P1) resulted from hydration in oedometric conditions under a low constant axial load of $\sigma_a = 21 \text{ kPa}$ applied by means of a dead weight. In order to minimise friction effects during the bentonite swelling, the surfaces in contact with the samples, as well as all sealing rings of the oedometric cell, were lubricated with grease. The second stress path (P2) involved isochoric wetting. An initial total axial stress of $\sigma_a = 190 \text{ kPa}$ was applied before wetting, in order to ensure a proper contact of the system parts. To prevent volume changes during hydration, the axial displacement was constantly monitored and corrected by increasing the axial stress. The maximum variation of axial strain allowed

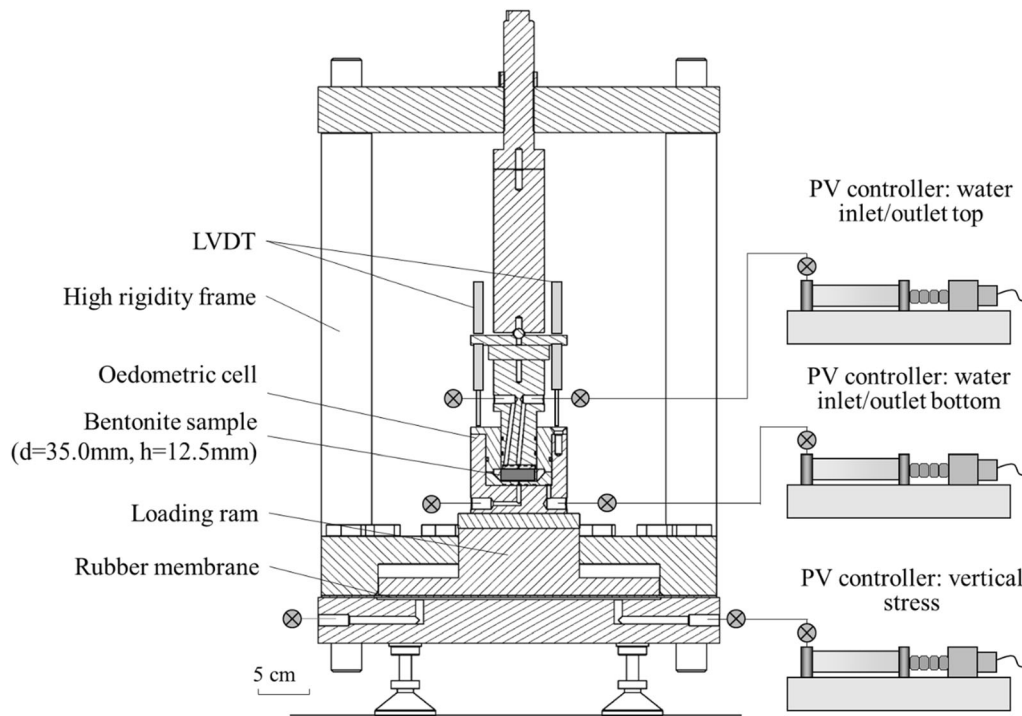


Fig. 3 Schematic layout of the high-pressure oedometric cell (after Ferrari et al. [9])

Table 1 Initial conditions of the samples

Sample	Water content (–)	Dry density (Mg/m^3)	Void ratio (–)	Degree of saturation (–)	Total suction (MPa)
P1-1	0.06	1.48	0.86	0.20	99.5
P1-2	0.06	1.47	0.87	0.19	98.7
P1-3	0.07	1.50	0.83	0.23	90.5
P2-1	0.06	1.49	0.85	0.20	104.2
P2-2	0.06	1.49	0.84	0.20	106.4
P2-3	0.06	1.49	0.84	0.20	105.0

was $\pm 0.6\%$, corresponding to a maximum variation of dry density of $\pm 0.01 \text{ Mg/m}^3$. For both series P1 and P2, once the equilibrium with the external water pressure ($u_w = 20 \text{ kPa}$) was reached, the samples were further subjected to loading in steps up to $\sigma_a = 20 \text{ MPa}$.

Table 2 summarises the experimental program; some of the samples were dismantled at intermediate stages of the paths in order to perform MIP and SEM analyses at various states of the hydro-mechanical loadings.

The MIP tests were carried out using a Thermo Electron Corporations MIP apparatus. The apparatus uses two operating units: a low-pressure (Pascal 140) and a high-pressure (Pascal 240) unit. In the first part of the test, the Pascal 140 was used. Vacuum was first applied inside the dilatometer, and the intrusion of mercury started at very low pressure. By the first filling of the dilatometer, the apparatus computed the volume of the sample. Incremental

increasing pressure was then applied to the mercury (max. pressure is 400 kPa), and the intruded volume was recorded by the unit. At the end of measurements on the low-pressure unit, the dilatometer was transferred onto the high-pressure unit where the pressure was increased up to 200 MPa, corresponding to a pore diameter of 7.5 nm. Most of the MIP experiments were repeated in order to evaluate the consistency of the test results. The results obtained on the twin specimens were very similar to each other and proved good reliability and accuracy of the measurements.

The SEM tests were performed in a high-performance scanning electron microscope FEI Quanta 200f. Observations were carried out in a high-vacuum mode using the secondary electron detector at an accelerating voltage between 20 and 30 kV. The applied working distance

Table 2 Stages of the experimental program

Path	Sample	Testing sequence	Microstructural analysis
1	P1-1	Saturation at constant $\sigma_a = 21\text{kPa}$	MIP, SEM
	P1-2	Saturation at constant $\sigma_a = 21\text{kPa}$; Compression $\sigma_a = 21\text{kPa} \rightarrow 3.2\text{MPa}$	MIP, SEM
	P1-3	Saturation at constant $\sigma_a = 21\text{kPa}$; Compression $\sigma_a = 21\text{kPa} \rightarrow 20\text{MPa}$	–
2	P2-1	Isochoric saturation; Compression $\sigma_a \rightarrow 20\text{MPa}$	–
	P2-2	Isochoric saturation	MIP-SEM
	P2-3	Isochoric saturation	–

amounted for 10–20 mm. SEM magnifications were in the range of 15–50,000 X.

4 Results and discussion

4.1 Hydro-mechanical response

The sign convention used to present the results follows that of Soil Mechanics, i.e. positive values stand for contractive strains and compression stress.

Figure 4 shows the evolution of axial displacement of the samples hydrated under low axial load. After an initial swelling rate that was rather the same for all samples, a deviation is observed between samples after 3 h of hydration and an axial strain of about -40%. Regardless of these deviations between tests, the final value of axial strain stabilised at around -80% for all samples.

The applied axial strains and developments of swelling pressure of the three samples subjected to wetting under isochoric conditions are represented in Fig. 5. In spite of

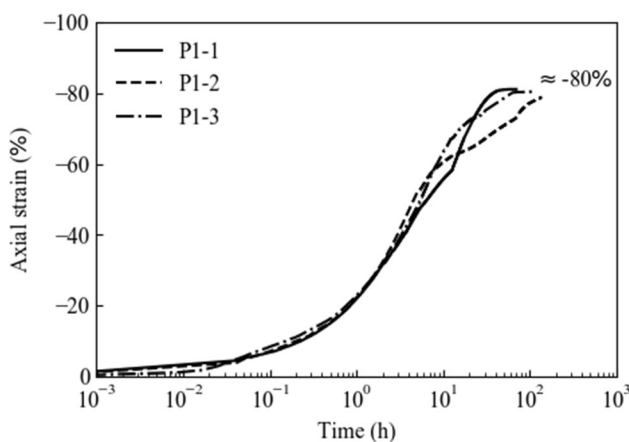


Fig. 4 Evolution of axial strain in time during hydration of the samples under low axial stress ($\sigma_a = 21\text{ kPa}$)

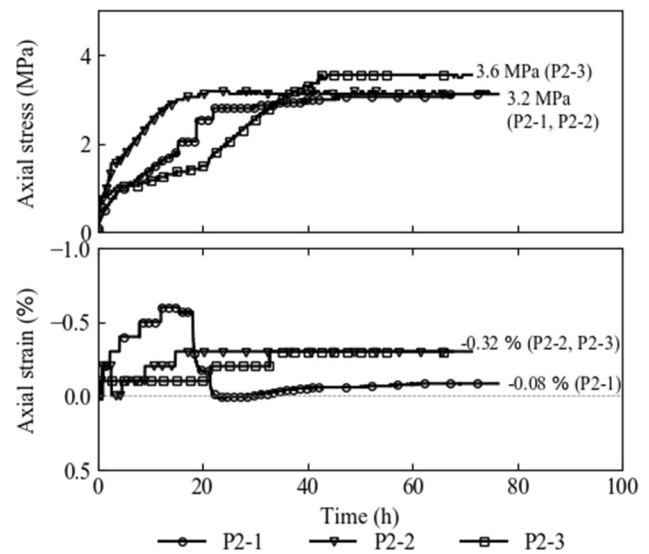


Fig. 5 Evolution of vertical stress applied and vertical strain in time during isochoric saturation

the different evolutions of stress and strains, the final value of the swelling pressure is fairly similar (3.2–3.6 MPa). In Fig. 6, the obtained results are compared to trends reported in the literature for the dependency of the swelling pressure on the dry density for MX80 bentonite prepared in different forms [4, 13, 24]. It appears that for a given dry density the initial compacted state of the bentonite does not influence the final value of swelling pressure. Similar conclusions on compacted MX80 powder bentonite were obtained in [27] when the presence of eventual gaps was accounted for in the computation of the dry density.

The consolidation curves obtained upon loading after saturation of samples P1-2, P1-3 and P2-1 are shown in Fig. 7. These curves allowed the estimation of the hydraulic conductivity using the analytical model presented in [9] that accounts for the non-instantaneous application of the loading. The computed hydraulic conductivity is shown in Fig. 8 as a function of dry density and

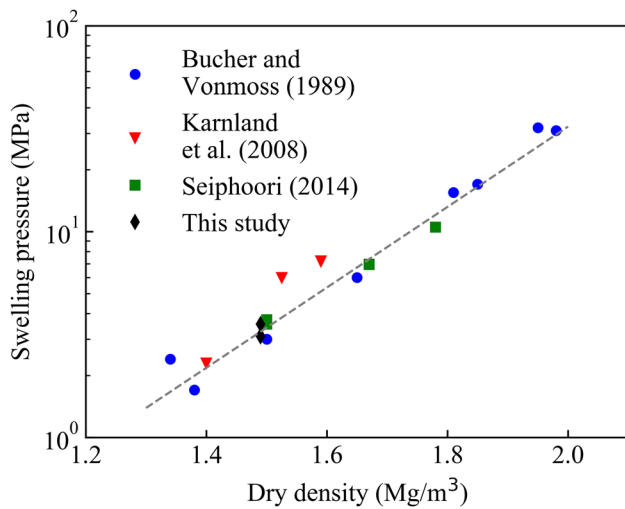


Fig. 6 Comparison of the swelling pressure obtained with the values reported in the literature (additional data from [4, 13, 24])

compared with those derived on the basis of direct measurements in saturated MX80 bentonite blocks [13, 30]. In spite of comparing direct measurements and indirect measurements, the unique trend appears satisfactory, also considering the differences in the values obtained within the same test campaign.

The results in terms of void ratio (corrected accounting for the deformation of the apparatus) vs. total axial stress (while maintaining a constant back-pressure of 20 kPa) for each sample are shown in Fig. 9. The samples hydrated at low confining stress equilibrated at a saturated void ratio between 2.25 and 2.35. Thus, in spite of slightly different

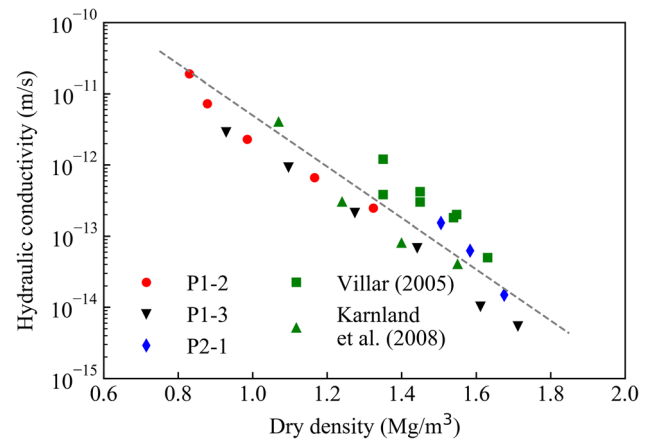


Fig. 8 Computed hydraulic conductivity as a function of dry density from the consolidation curves. The values obtained by Villar [30] and Karnland et al. [13] on compacted saturated MX80 bentonite are shown for comparison purposes

evolutions of the axial strain with time (Fig. 4), the initial state for the loading paths was similar for all samples.

For samples P1-2 and P1-3, a rather stiff response was obtained upon compression up to 0.2–0.5 MPa, with a corresponding index $C_s = -\Delta e / \Delta(\log \sigma'_a)$ of 0.05 for sample P1-2 and 0.08 for sample P1-3. Although the low compressibility could be surprising in view of the high void ratio attained after the swelling, it can be explained accounting for the evolution of the radial stress during the saturation phase. Sivakumar et al. [26] measured radial stresses developed in clays wetted under different loading conditions, pointing out an increase in the lateral pressure coefficient (evaluated by the authors in terms of total

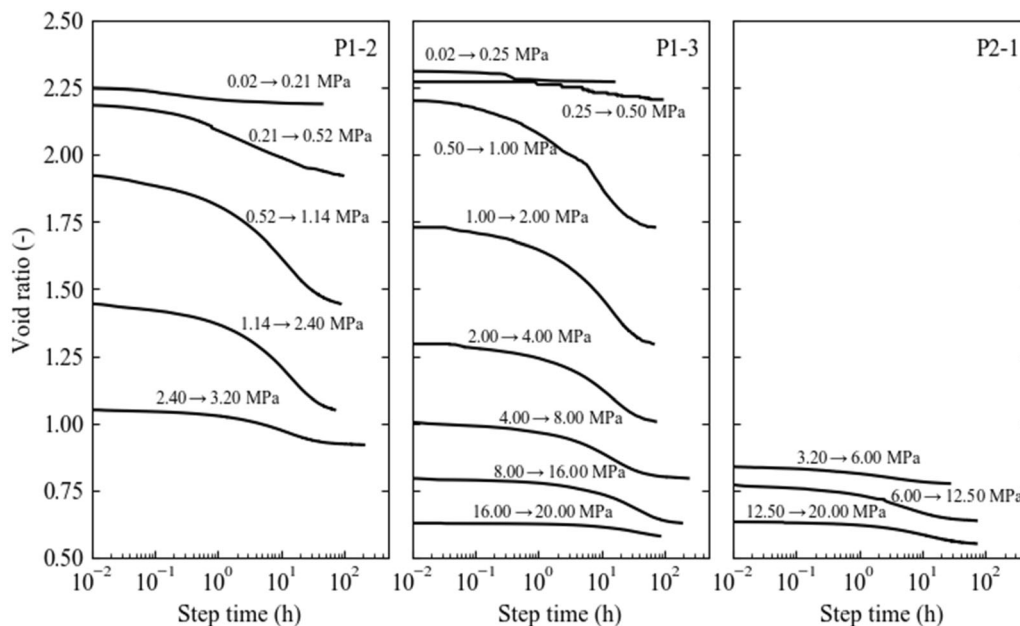


Fig. 7 Consolidation curves of the compression stages after saturation. The inserts indicate the initial and final loads of each stage in MPa

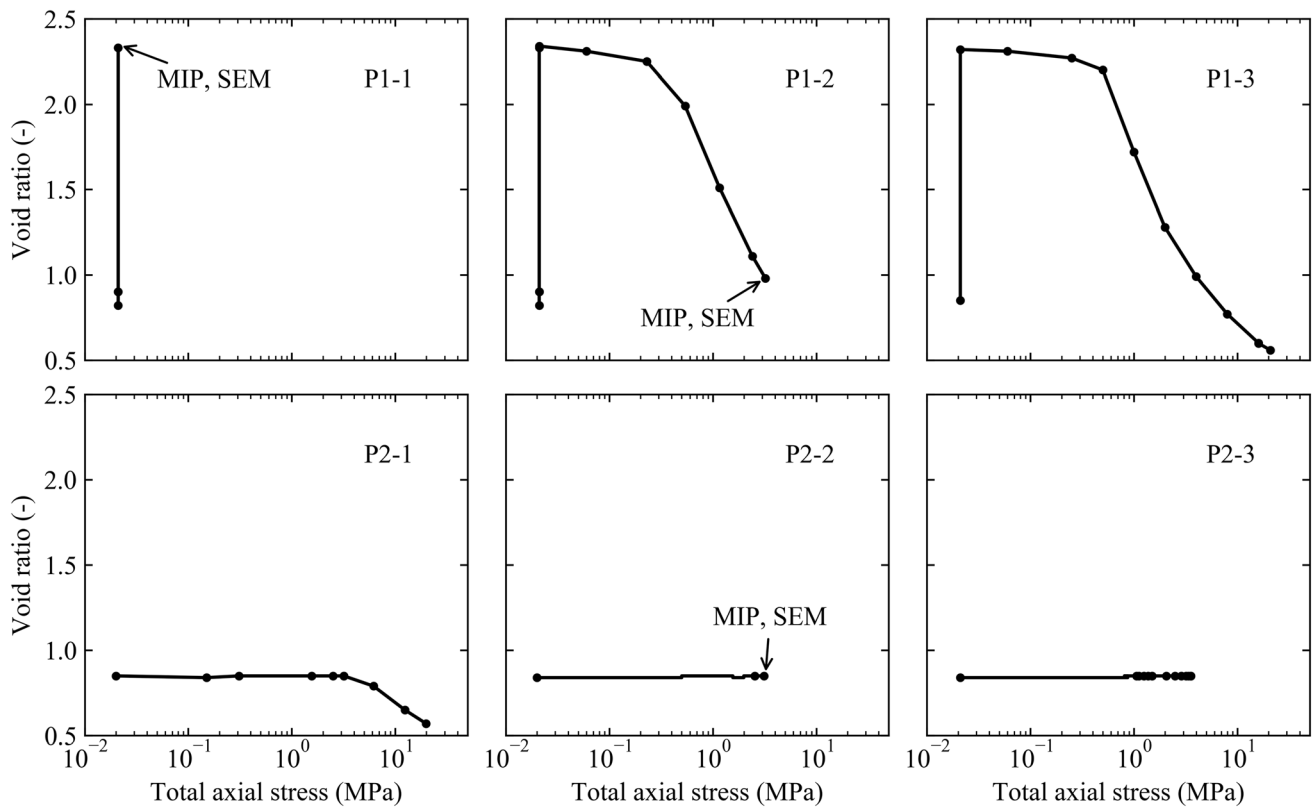


Fig. 9 Results of the tests in terms of void ratio vs. total axial stress

stress) with the increase in the activity of the tested clays, as well as for lower values of applied vertical stress. For the tested MX-80 bentonite with a high activity and low axial stress, the development of high radial stresses relative to the axial load during wetting is expected, with a consequent increase in the deviatoric stress. These loading conditions along with the contraction of the yield surface associated with wetting may cause the material to yield. However, in the subsequent stage the axial loading causes a change in the stress-path direction that can explain the high stiffness. When the axial loading is sufficiently increased (0.2 MPa for P1-2 and 0.5 MPa for P1-3), a new yielding state during compression is attained.

The role of the deviatoric stress developed during the wetting process on the vertical yield stress can be seen in Fig. 10, which shows the compression curve of sample P1-3 together with compression after swelling tests reported by Villar [30] and Tang and Cui [29]. Villar [30] saturated a MX-80 bentonite block under a vertical load of 0.1 MPa under oedometric conditions, and Tang and Cui [29] saturated a sample of compacted MX80 bentonite under a constant isotropic stress of 0.1 MPa. The axial load during saturation was the same in both cases, which implies that differences in the stress state between the two tests correspond to the deviatoric stress. The influence of oedometric conditions can be inferred by comparing the initial

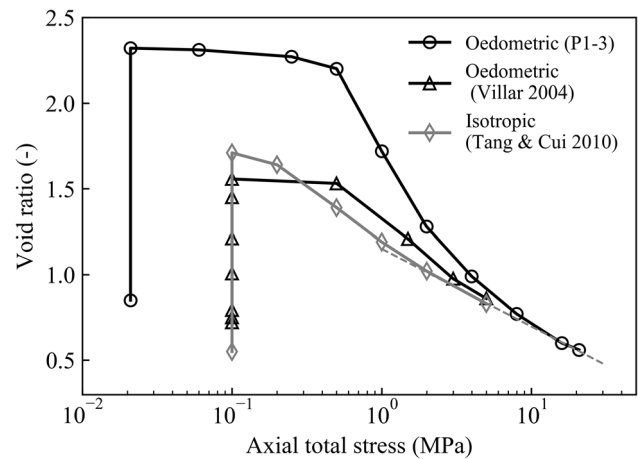


Fig. 10 Compression curve of sample P1-3 obtained in the present study under oedometric conditions and data obtained by Villar [30] under oedometric conditions and Tang & Cui [29] on isotropic compression. All samples were saturated under low constant stress in the initial stage (vertical line in the plot)

compression stage of the oedometric tests with the isotropic test, which showed different stiffness at low stresses. These differences decrease progressively with increasing stress applied during hydration, until reaching a similar volumetric response at high stresses.

Subsequent compression of sample P1-3 led to a non-linear response in the plane axial stress-void ratio (Fig. 9). A similar trend of compression for a saturated bentonite with a high initial void ratio was also reported in [18].

The final void ratios of samples P1-2 ($e = 0.98$) and P2-2 ($e = 0.85$) were different despite being both saturated and subjected to the same value of final axial stress of 3.2 MPa. There is therefore a dependency of the void ratio on the stress path followed. Nevertheless, the dependency of the volumetric behaviour from the previous stress path decreases during the subsequent loading stage. This can be observed in Fig. 11, which compares the compression curves of samples P1-3 and P2-1. The difference in void ratio for a given axial stress decreases as loading increased, and once axial stress exceeded 12 MPa, both samples followed the same virgin compression curve (depicted here in terms of total stress due to the limited value of applied back-pressure). This result supports the modelling hypothesis presented in [3] that the virgin compression curve at saturation is not affected by the initial fabric or stress path to saturation.

4.2 Microstructural observations

The MIP and SEM tests were performed on freeze-dried sub-cores that were obtained from each sample at its final state. The freeze-drying was preferred to other preparation techniques because of the very limited effect on the original structure of the clayey samples [8].

In the present study, the distinction between the intra- and inter-assemblage porosity is done based on the intrusion/extrusion cycles of the MIP technique, following the method proposed by Delage and Lefebvre [6], which as discussed by Romero et al. [20] represents an objective criterion. The method consists in identifying the volume of

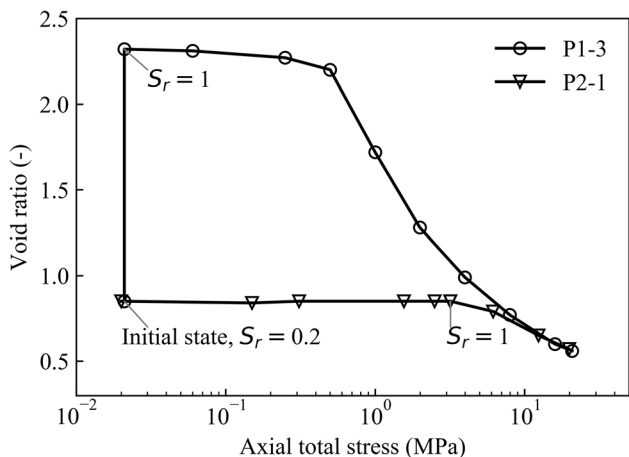


Fig. 11 Results of the oedometric compression tests after saturation under constant axial stress (P1-3) and constant volume conditions (P2-1)

mercury that is not recovered at the end of the intrusion–extrusion cycle as the volume corresponding to intra-assemblage porosity. Figure 12 shows the intruded and extruded void ratio with mercury for each sample as a function of the pore entrance diameter, as well as the limit between intra- and inter-assemblage porosity, which is identified from the final extruded void ratio projected into the intrusion curve. Thus, according to Fig. 12, pores with

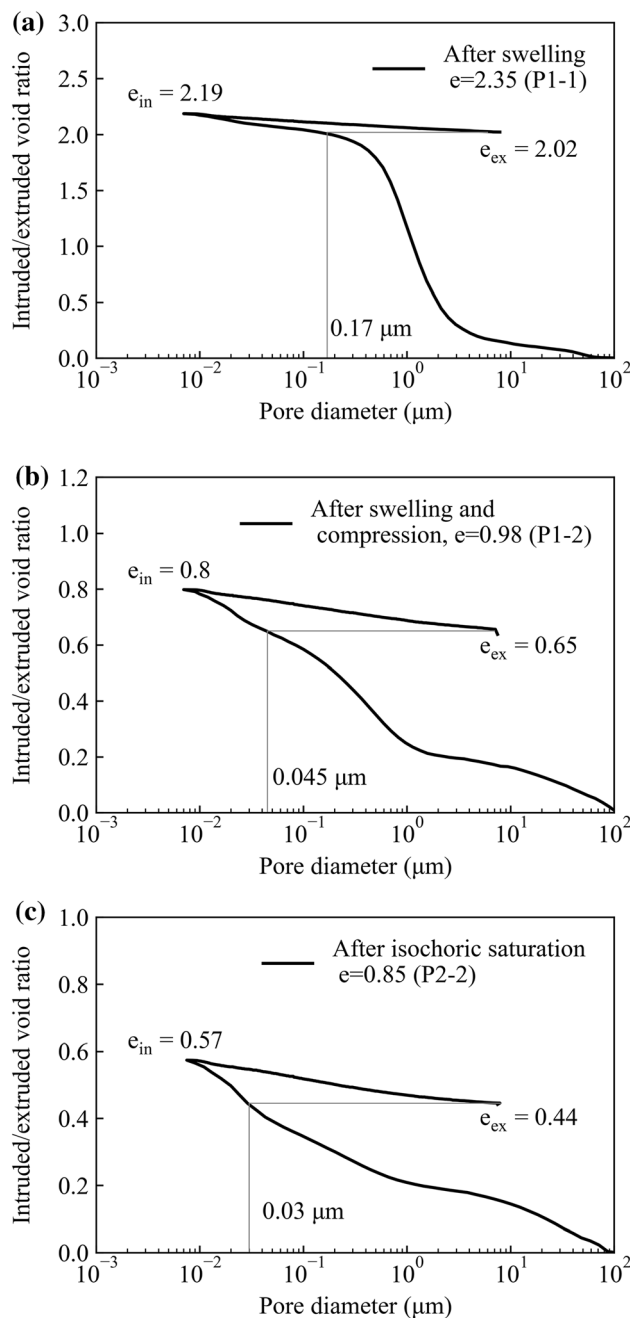


Fig. 12 Void ratio intruded and extruded by MIP technique as a function of the computed pore diameter. **a** sample P1-1, **b** sample P1-2 and **c** sample P2-2. For each case, the distinction between intra- and inter-aggregate is displayed

diameter below $0.03 \mu\text{m}$ belong to intra-assemblage porosity in all samples. This value increases up to $0.17 \mu\text{m}$ for the sample P1-1, which after free axial swelling had a total void ratio of $e = 2.35$. For the free swollen sample and later compressed to the isochoric swelling pressure (sample P1-2), the pore size delimiting intra- and inter-assemblage porosities is around $0.045 \mu\text{m}$.

As seen in Fig. 2, in the as-poured state the PSD is bimodal, with peaks around $0.01 \mu\text{m}$ (intra-assemblage) and $16 \mu\text{m}$ (inter-assemblage). In order to visualise the effects of saturation, the PSD of the samples P1-1 and P2-2 can be compared to the PSD of the initial as-poured state in Fig. 13. After saturation, the PSD changed significantly. The PSD of the sample saturated under low axial load (P1-1, Fig. 13a) had one major mode, which is a typical feature exhibited by active clays after swelling under moderate or no confinement (e.g. [17, 22, 23]). This mode is not present in the as-poured state and it is related to the development of inter-assemblage porosity (i.e. pore diameter $> 0.17 \mu\text{m}$). The resulting homogeneity in terms of PSD can be clearly

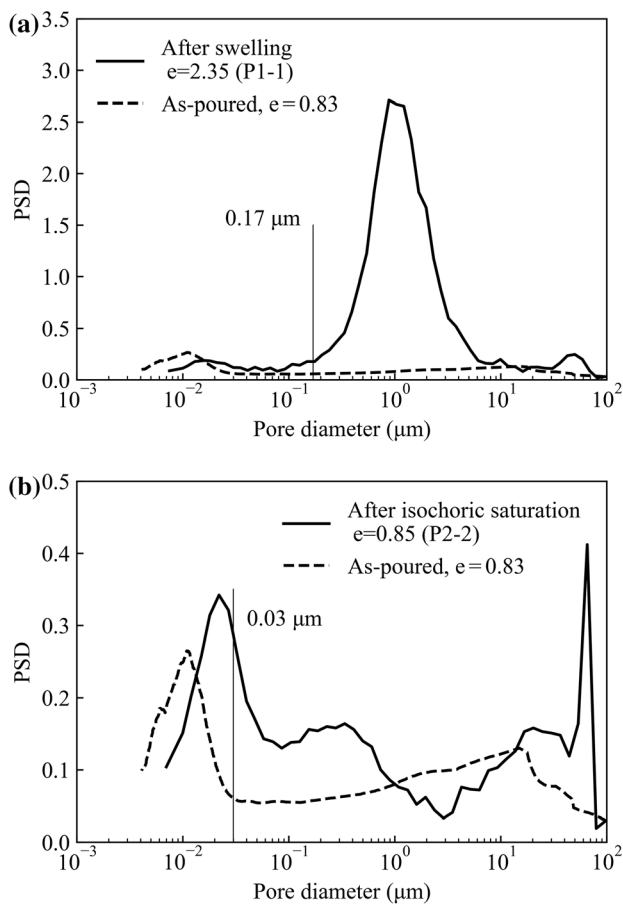


Fig. 13 **a** PSD of P1-1 sample saturated under constant low axial stress ($\sigma_a = 21 \text{ kPa}$), and the granular MX80 in as-poured state. **b** PSD of P2-2 sample saturated under isochoric conditions and the as-poured state. The as-poured state was reported in [24]

observed in the SEM images (Fig. 14a) where no outlines of the initial granular structure are observed.

After isochoric saturation, the PSD of the sample P2-2 displayed a multimodal porosity (Fig. 13b). Comparing the PSD to that of the as-poured state, the peak around $0.02 \mu\text{m}$ can be associated with a partial swelling of the assemblages within the inter-grain pores. A new porosity class (with diameters in the range of $0.1\text{--}1 \mu\text{m}$) emerges

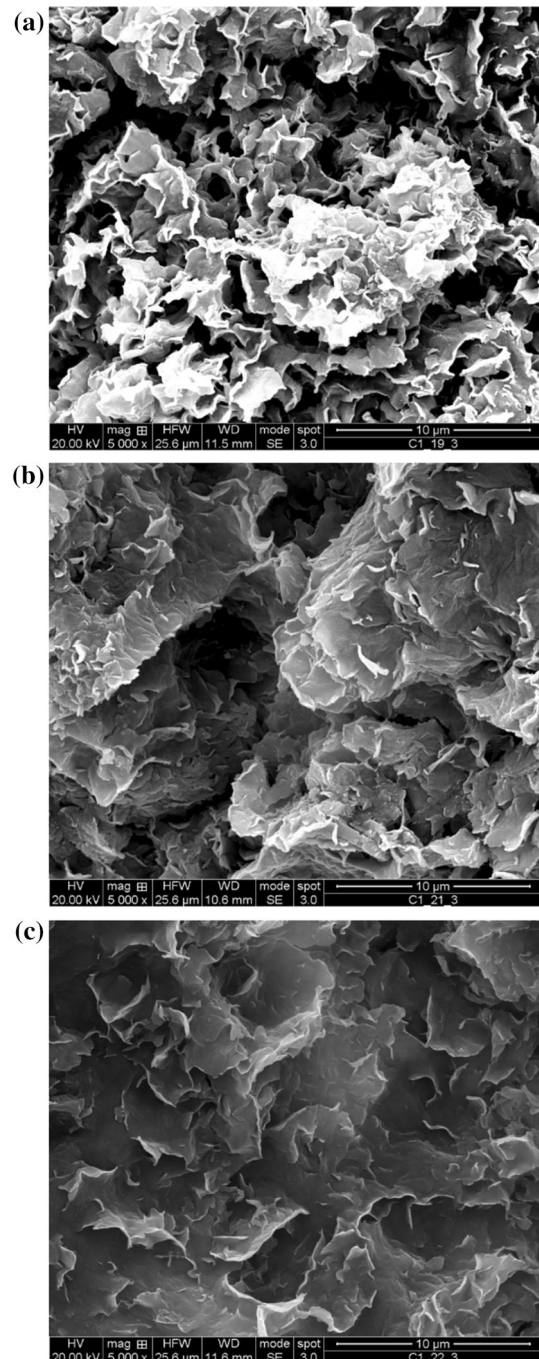


Fig. 14 SEM photomicrographs of **a** sample P1-1, **b** sample P2-2 and **c** sample P1-2. The total width of the pictures corresponds to $25.6 \mu\text{m}$

after saturation within the inter-assembly porosity domain, which was also observed in granular mixtures of FEBEX bentonite pellets [2]. Pores larger than 40 μm are mostly related to cracks resulting from freeze-drying. A comparison with the sample P1-1 reveals that isochoric conditions upon saturation enhance the development of larger intra-assembly pores and lead to a more heterogeneous fabric. The heterogeneity of the resulting fabric in these conditions is also observed in the SEM images shown in Fig. 14b, where the presence of the different pore size modes can be easily visualised.

Figure 15 shows the PSD of sample P1-2, saturated in free swelling conditions and compressed up to the swelling pressure ($\sigma_a = 3.2$ MPa), together with the PSD of samples P1-1 and P2-2. An increase of the intra-assembly pore volume is observed upon compression, along with a pronounced decrease in the inter-assembly pore sizes. This change in intra-assembly porosity is in contrast to what is usually observed after compression in unsaturated conditions, where the intra-assembly volume tends to slightly decrease [2, 16]. This result indicates that the saturation state has an influence on the mechanical interaction between porosity levels. Considering that the final void ratio of sample P1-2 was still higher than the one of the sample P2-2, the comparison of the three curves suggests that upon compression the PSD after swelling tends to evolve towards the PSD developed after isochoric saturation (sample P2-2). The SEM picture of sample P1-2 is presented in Fig. 14c, showing higher homogeneity compared to the sample P2-2 (Fig. 14b).

Both MIP and SEM observations demonstrate that depending on the stress path different microstructural arrangements are achieved. Nevertheless, the MIP results

indicate that under continued compression at saturated states the material tends towards a unique PSD, which is consistent with the macrostructural results that showed convergence towards a unique volumetric compressive behaviour.

5 Conclusions

The objectives of this study were to examine the response and the evolution of fabric for granular bentonite subjected to two different stress paths that shared the same initial and final stress-saturation states. The first stress path consisted in saturation under low vertical stress followed by compression and the second path involved saturation under constant volume conditions and subsequent compression.

The results showed that after saturation under low constant stress, a vertical stress higher than the swelling pressure (as obtained from the sample that was saturated under constant volume conditions) is needed to recover the initial void ratio. The initial compression stage of the sample that was subjected to saturation under constant stress showed a relatively stiff response. This was interpreted as the result of the high ratio between radial and axial stresses during wetting and one-dimensional swelling. Further compression under saturated states for both paths led to the same volumetric behaviour that defines the virgin compression behaviour of clay, suggesting that this is an intrinsic relationship for saturated MX80 bentonite, regardless of the stress path followed to reach saturation.

Inspection of the MIP results showed that the two saturated samples subjected to the same vertical stress shared the same modes of porosity. However, the intra-assembly

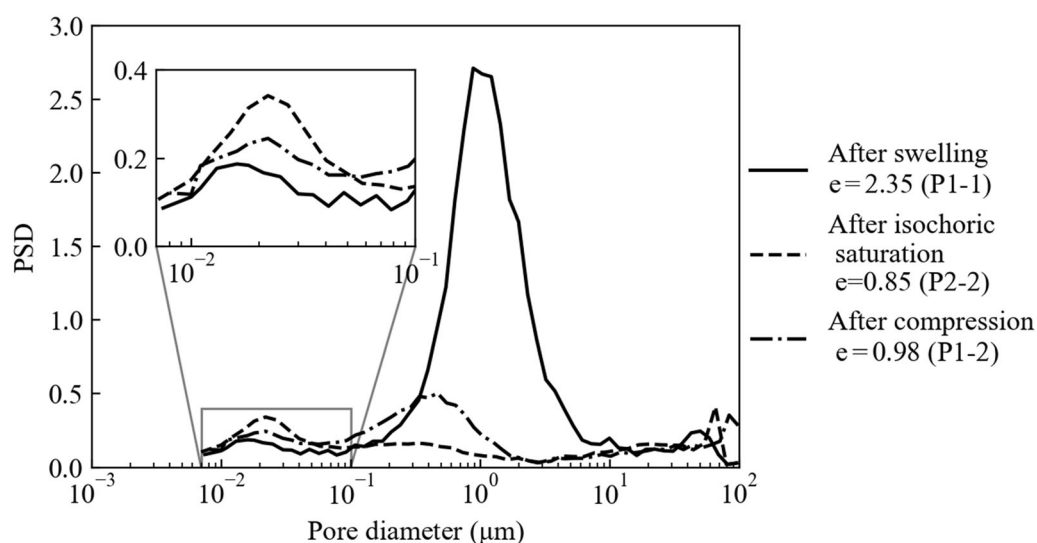


Fig. 15 PSD function of samples P1-1 (after free swelling), P1-2 (free swelling and compressed up to the swelling pressure) and P2-2 (after isochoric saturation)

porosity of the sample saturated under constant volume occupied a larger proportion than in the sample saturated at low constant load and compressed to the swelling pressure. The bimodal structure of bentonite is thus progressively recovered upon compression. These observations at the microstructural level can be used to further develop constitutive models based on multiporosity concepts.

Acknowledgements This work has received funding from the Euratom research and training programme 2014–2018 under Grant Agreement No 745942. The authors are also grateful for the financial support from NAGRA (Swiss national cooperative for nuclear waste storage).

Funding Open access funding provided by EPFL Lausanne.

Open Access This article is licensed under a Creative Commons Attribution 4.0 International License, which permits use, sharing, adaptation, distribution and reproduction in any medium or format, as long as you give appropriate credit to the original author(s) and the source, provide a link to the Creative Commons licence, and indicate if changes were made. The images or other third party material in this article are included in the article's Creative Commons licence, unless indicated otherwise in a credit line to the material. If material is not included in the article's Creative Commons licence and your intended use is not permitted by statutory regulation or exceeds the permitted use, you will need to obtain permission directly from the copyright holder. To view a copy of this licence, visit <http://creativecommons.org/licenses/by/4.0/>.

References

1. Agus SS, Schanz T (2008) A method for predicting swelling pressure of compacted bentonites. *Acta Geotech* 3(2):125–137
2. Alonso EE, Romero E, Hoffmann C (2011) Hydromechanical behaviour of compacted granular expansive mixtures: experimental and constitutive study. *Géotechnique* 61(4):329–344
3. Bosch JA, Ferrari A, Laloui L (2021) Coupled hydro-mechanical analysis of compacted bentonite behaviour during hydration. *Comput Geotech* 140:104447
4. Bucher F, Müller-Vonmoos M (1989) Bentonite as a containment barrier for the disposal of highly radioactive waste. *Appl Clay Sci* 4:157–177
5. Darde B, Roux JN, Pereira JM, Dangla P, Talandier J, Vu MN, Tang AM (2020) Investigating the hydromechanical behaviour of bentonite pellets by swelling pressure tests and discrete element modelling. *Acta Geotech* 16:507–524
6. Delage P, Lefebvre G (1984) Study of the structure of a sensitive Champlain clay and its evolution during consolidation. *Can Geotech J* 21(1):21–35
7. Delage P, Marcial D, Cui YJ, Ruiz X (2006) Ageing effects in a compacted bentonite: a microstructure approach. *Geotechnique* 56(5):291–304
8. Delage P, Pellerin FM (1984) Influence de la lyophilisation sur la structure d'une argile sensible du Québec. *Clay Miner* 19(2):151–160
9. Ferrari A, Favero V, Laloui L (2016) One-dimensional compression and consolidation of shales. *Int J Rock Mech Min Sci* 88:286–300
10. Gens A, Alonso EE (1992) A framework for the behavior of unsaturated expansive clays. *Can Geotech J* 29:1013–1032
11. Guerra AM, Cui YJ, Mokni N, Delage P, Bornert M, Aïmedieu P, Tang AM, Bernier F (2018) Investigation of the hydro-mechanical behaviour of a pellet/powder MX80 bentonite mixture using an infiltration column. *Eng Geol* 243:18–25
12. Hoffmann C, Alonso EE, Romero E (2007) Hydro-mechanical behaviour of bentonite pellet mixtures. *Phys Chem Earth Parts A/B/C* 32:832–849
13. Karnland O, Nilsson U, Weber H, Wersin P (2008) Sealing ability of Wyoming bentonite pellets foreseen as buffer material—laboratory results. *Phys Chem Earth Parts A/B/C Clays Nat Eng Barriers Radioact Waste Confin* 33:S472–S475
14. Li Z, Su G, Zheng Q, Nguyen TS (2020) A dual-porosity model for the study of chemical effects on the swelling behaviour of MX-80 bentonite. *Acta Geotech* 15(3):635–653
15. Liu ZR, Cui YJ, Ye WM, Chen B, Wang Q, Chen YG (2020) Investigation of the hydro-mechanical behaviour of GMZ bentonite pellet mixtures. *Acta Geotech* 15:2865–2875
16. Lloret A, Villar MV, Sanchez M, Gens A, Pintado X, Alonso EE (2003) Mechanical behaviour of heavily compacted bentonite under high suction changes. *Geotechnique* 53(1):27–40
17. Manca D, Ferrari A, Laloui L (2016) Fabric evolution and the related swelling behaviour of a sand/bentonite mixture upon hydro-chemo-mechanical loadings. *Géotechnique* 66(1):41–57
18. Marcial D, Delage P, Cui YJ (2002) On the high stress compression of bentonites. *Can Geotech J* 39(4):812–820
19. Niu W, Ye W, Song X (2020) Unsaturated permeability of Gaomiaozi bentonite under partially free-swelling conditions. *Acta Geotech* 15:1095–1124
20. Plötze M, Weber H P (2007) ESDRED: emplacement tests with granular bentonite MX-80. *Nagra Arbeitsbericht NAB*, 7.
21. Pusch R (1982) Mineral-water interactions and their influence on the physical behavior of highly compacted Na bentonite. *Can Geotech J* 19:381–387
22. Romero E, Della Vecchia G, Jommi C (2011) An insight into the water retention properties of compacted clayey soils. *Géotechnique* 61(4):313–328
23. Rosone M, Airò Farulla C, Ferrari A (2016) Shear strength of a compacted scaly clay in variable saturation conditions. *Acta Geotech* 11:37–50
24. Seiphoori A (2014) Thermo-hydro-mechanical characterisation and modelling of MX-80 granular bentonite. PhD Thesis École Polytechnique Fédérale de Lausanne.
25. Seiphoori A, Ferrari A, Laloui L (2014) Water retention behaviour and microstructural evolution of MX-80 bentonite during wetting and drying cycles. *Géotechnique* 64(9):721–734
26. Sivakumar V, Zaini J, Gallipoli D, Solan B (2015) Wetting of compacted clays under laterally restrained conditions: initial state, overburden pressure and mineralogy. *Géotechnique* 65(2):111–125
27. Su W, Wang Q, Ye WM, Deng YF, Chen YG (2021) Swelling pressure of compacted MX80 bentonite/sand mixture prepared by different methods. *Soils Found* 61(4):1142–1150
28. Sun H, Mašin D, Najser J, Neděla V, Navrátilová E (2020) Fractal characteristics of pore structure of compacted bentonite studied by ESEM and MIP methods. *Acta Geotech* 15:1655–1671
29. Tang AM, Cui YJ (2010) Experimental study on hydro-mechanical coupling behaviours of highly compacted expansive clay. *J Rock Mech Geotech Eng* 2(1):39–43
30. Villar MV (2005) MX-80 Bentonite. Thermal-hydro-mechanical characterisation performed at CIEMAT in the context of the prototype project (No. CIEMAT–1053). Centro de Investigaciones Energeticas
31. Wang Q, Cui YJ, Tang AM, Barnichon JD, Saba S, Ye WM (2013) Hydraulic conductivity and microstructure changes of compacted bentonite/sand mixture during hydration. *Eng Geol* 164:67–76

32. Wang Q, Tang AM, Cui YJ, Delage P, Barnichon JD, Ye WM (2013) The effects of technological voids on the hydro-mechanical behaviour of compacted bentonite–sand mixture. *Soils Found* 53(2):232–245

Publisher's Note Springer Nature remains neutral with regard to jurisdictional claims in published maps and institutional affiliations.